Room Temperature Triethylamine Sensor Based on Reduced Graphene Oxide/CeO_2 Nanocomposites

*Cecilia A. Zito, Tarcísio M. Perfecto, Diogo P. Volanti**

Laboratory of Materials for Sustainability (LabMatSus), São Paulo State University (UNESP), Rua Cristóvão Colombo 2265, 15054-000 São José do Rio Preto, Brazil

*Corresponding author. E-mail: diogo.volanti@unesp.br

ABSTRACT

Triethylamine (TEA) detection has been widely performed by using chemoresistive sensors. Nevertheless, chemoresistive sensors still exhibit limitations to be addressed in terms of power consumption and humidity interference, and developing efficient TEA sensors operated at low temperatures and humid conditions remains a challenge. Here, we present the effect of reduced graphene oxide (RGO) on the TEA sensing performance of CeO_2 nanospheres at room temperature and relative humidity (RH) range of 34-70%. We show that CeO_2 is a suitable sensing material for TEA detection at room temperature and humidity conditions; however, the modification with RGO greatly improves the TEA-sensing performance. The RGO/CeO_2 nanocomposite has higher sensitivity and selectivity to TEA than the bare CeO_2-based sensor, in addition to the low theoretical detection limit of 1 ppm at 70% RH. Moreover, we elucidate that humidity plays a positive role in the detection of TEA. Our findings elucidate that RGO positively affects the sensing performance of CeO_2 nanospheres, which can be attributed to the improvements in the baseline electrical resistance and enhancement of the active sites for TEA adsorption due to the RGO modification. This work provides a promising strategy for developing sensitive TEA sensors with practical applications.

KEYWORDS

ceria, cerium dioxide, chemoresistive, humidity, volatile organic compounds, microwave-assisted synthesis

1. INTRODUCTION

Volatile organic compounds (VOCs) can be found in indoor and outdoor air environments [1] due to their ample use in manufacturing processes and materials.[2] The concerns surrounding VOCs arise from their potential adverse effects on human health.[2] Among the VOCs, triethylamine (TEA) is one pollutant with toxic and odorous characteristics, which has several industrial applications ranging from organic solvent to catalyst.[3,4] According to the Occupational Safety and Health Administration (OSHA), the exposure limit for TEA is 25 ppm during an 8-hour workday.[5] Exposure to TEA may lead to headaches, eye irritation, dizziness, and respiratory discomfort.[6–8] Therefore, real-time monitoring of TEA levels is required for air quality and human safety.

The detection of TEA has been extensively performed by using chemoresistive sensors based on semiconducting metal oxides (SMOx), including SnO_2, [9] $ZnSnO_3$,[10] ZnO,[11] In_2O_3,[12] WO_3,[13] Co_3O_4,[14] and NiO.[15] Despite the great TEA-sensing properties of such sensors, they often require high operating temperatures (above 180 °C),[14,16,17] causing an increase in the power consumption and costs of the sensing device. Another major drawback of chemoresistive sensors is the worsening of the TEA-sensing performance due to humidity, which leads to a clear and significant suppression of the sensor signal when increasing humidity levels.[17–20]

The preparation of nanocomposites, control of oxygen vacancies, metal doping/loading, or hydrophobic modifications are among the strategies to develop SMOx-based sensors that can either operate at room temperature (RT) or have humidity-tolerance properties.[21–24] Yet, sensors operated at low temperatures still exhibit low TEA signals under humid environments,[25,26] while the sensors with humidity resistance require heating at elevated temperatures.[27,28] It is still challenging to overcome both limitations for TEA sensors simultaneously.[29]

Incorporating reduced graphene oxide (RGO) into SMOx nanostructures not only enables the sensor operation at RT due to the good electrical conductivity [21,30] but also leads to general improvements in the TEA-sensing performance. Nanocomposites based on RGO/SMOx have a lower operating temperature, improved selectivity, and higher sensor signal to TEA than bare SMOx.[31–33]

In this sense, RGO can be combined with a suitable SMOx to produce a high-performance sensor. Studies have demonstrated that pristine CeO_2 is a viable sensing material

to detect different gases and compounds at reduced working temperatures in humid conditions, [34–38] Formerly, we observed that humidity plays a positive role in the sensing performance of CeO_2-based sensors for the detection of TEA and CO_2.[36,37] However, the study of the synergistic effect between RGO and CeO_2 has been explored so far for the detection of a few inorganic gases, mainly NO_2,[39–41] whereas VOCs detection remains barely explored.

Herein, we demonstrate the effect of the modification with RGO on the TEA-sensing performance of CeO_2 nanospheres. Unlike many SMOx, both developed sensors, bare CeO_2 and RGO/CeO_2, present high sensor signals to TEA at RT and relative humidity (RH) between 34% and 70%. Yet, the RGO/CeO_2 nanocomposite has higher sensitivity and selectivity to TEA than CeO_2 nanospheres, in addition to the great calculated detection limit of 1 ppm at 70% RH. Our findings confirm that humidity positively influences the TEA-sensing performance of CeO_2 nanostructures; however, the sensing properties are greatly improved after the modification with RGO. Hence, we show that the fabrication of RGO/CeO_2 nanocomposite is a promising approach for developing TEA sensors.

2. EXPERIMENTAL SECTION

2.1 Materials

$Ce(NO_3)_3.6H_2O$ (>99% purity) and urea (≥99.0 purity) were purchased from Sigma-Aldrich and the aqueous solution of H_2O_2 (30% w/w) from Vetec. All chemicals were used without further purification. The syntheses were performed using high-purity water (resistivity of 18.2 MΩ·cm at 25 °C), which was obtained from a Millipore Direct-Q® 3 UV Water Purification System.

2.2 Synthesis of the CeO_2/RGO nanocomposites

Graphene oxide (GO) was used as a precursor of the RGO/CeO_2 nanocomposite. GO was first synthesized from graphite powder by a modified Hummers' method,[30,42] then GO was modified by an additional chemical oxidation step, according to our previous report.[43]

The RGO/CeO_2 nanocomposite was synthesized *via* a one-step microwave-assisted hydrothermal method, by using an adaptation of a formerly reported method.[44] First, 21.8 mg of GO was dispersed in 75 mL of deionized water by using an ultrasonic bath for 1 h. Then,

$Ce(NO_3)_3.6H_2O$ (0.4531 g, 1.04 mmol) and urea (0.4744 g, 7.90 mmol) were dissolved in the mixture and H_2O_2 solution (800 µL) was added. The mixture was stirred for 20 min and then transferred to a 100 mL polytetrafluoroethylene (PTFE) container, sealed in a PTFE autoclave with a stainless-steel seal, and heated at 160 °C for 2 h in a microwave system (2.45 GHz/800 W).[45] The precipitate was centrifuged, washed with deionized water (6x) and ethanol (1x), and dried at 85 °C for 3 h. The same method was employed to synthesize the CeO_2 nanospheres, except for the addition of GO. The synthesis process of the RGO/CeO_2 nanocomposite is schematically illustrated in Figure 1.

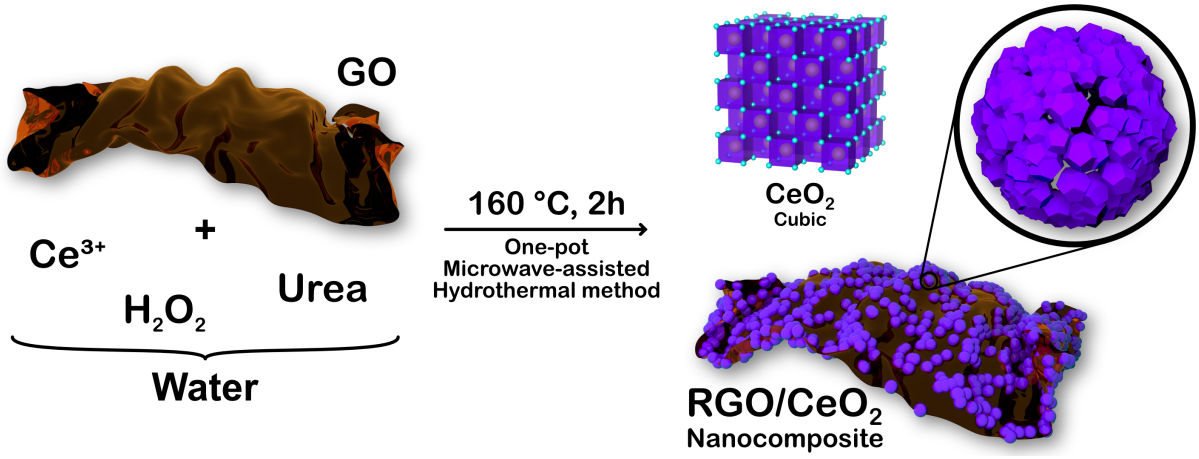

Figure 1. Schematic illustration of the synthesis of the RGO/CeO_2 nanocomposite *via* the microwave-assisted hydrothermal method.

2.3 Characterization

Powder X-ray diffraction (PXRD) analysis was performed on a Rigaku MiniFlex 300 powder diffractometer using Cu Kα radiation (λ=1.5418 Å), operated at 30 kV and 10 mA. Field-emission scanning electron microscopy (FESEM) and energy-dispersive X-ray spectroscopy (EDS) analyses were performed using a JEOL JSM-7500F microscope operated at 2 and 10 kV for the corresponding analyses. Transmission electron microscopy (TEM) and high-resolution TEM (HRTEM) images were obtained using a JEOL JEM2100F microscope operated at an accelerating voltage of 200 kV. Raman spectra were collected employing a HORIBA T64000 triple grating spectrometer with a laser excitation of 633 nm. X-ray photoelectron spectroscopy (XPS) analysis was carried out on a Thermo Scientific K-Alpha Spectrometer applying Al Kα X-ray radiation (1486.6 keV). The spectra were calibrated with the reference to the C 1s peak (284.8 eV). Attenuated total reflection Fourier transform infrared (ATR-FTIR) spectra were

recorded on a PerkinElmer Spectrum Two™ spectrometer. N_2 adsorption isotherms were measured at 77 K on a Micromeritics' Gemini® VII 2390 surface area analyzer. The specific surface areas were calculated using the Brunauer-Emmet-Teller (BET) method.

2.4 VOC-sensing measurements

The samples were dispersed in isopropanol by using an ultrasonic bath for 15 min. The dispersions at a concentration of around 20 mg mL^{-1} were deposited into alumina substrates containing interdigitated gold electrodes (100 μm wide lines and 100 μm spacing between the lines). The substrates containing the samples were heated at 150 °C for 1 h 10 min to stabilize the sensing layer.

The VOC-sensing measurements were performed at RT (24 °C). The prepared sensors were individually placed inside a 3D printed chamber made of polymeric material,[46] and connected to a Source Measure Unit (Keithley SourceMeter 2400). A combination of flow tube rotameters (Aalborg Instruments & Controls, Inc.) was employed to control the concentration of different VOCs and the RH levels at a constant flow of 200 mL min^{-1}. The sensors were kept under humid air flow before VOCs exposure to obtain a stable baseline. The RH was measured in the gas outlet of the testing chamber by using a thermohygrometer (HANNA, HI9564 model). The changes in the resistance of the sensors after VOC exposure were measured by employing a Source Measure Unit (Keithley SourceMeter 2400), applying a voltage of 20 V. The sensor signal was defined as the ratio R_0/R_{VOC}, where R_0 is the resistance in clean humid air and R_{VOC} is the resistance measured after VOC exposure. The response time is the time to reach 90% of the maximum resistance change after the sensor is exposed to the VOC, whereas the recovery time is defined as the time to recover 90% of the initial resistance after the exposure to the VOC.

3. RESULTS AND DISCUSSION

3.1 Characterization

We investigate the morphology of the CeO_2 and RGO/CeO_2 nanocomposite with FESEM and TEM (Figure 2). Pure CeO_2 is composed of spherical nanostructures with an average diameter of 100 nm, as shown in Figure 2a. The FESEM image of the RGO/CeO_2 nanocomposite (Figure 2b) reveals that the spherical morphology of CeO_2 is preserved; however, the CeO_2 nanospheres of *ca.* 150 nm are anchored on RGO sheets, which present a wrinkled surface. The TEM characterization confirms the existence of nanospheres with smaller diameters than those measured in FESEM images. The TEM image in Figure 2c provides a better understanding of the structure of a single CeO_2 nanosphere. The individual nanosphere is composed of small crystalline nanoparticles with a size ranging from 5 to 8 nm. The TEM image of the RGO/CeO_2 nanocomposite (Figure 2d) also elucidates that the CeO_2 nanosphere is composed of small particles with a size of 4.5–7 nm. However, the nanosphere is connected to a thin layer with a low degree of order, which can be assigned to the RGO. As shown in the HRTEM image of pure CeO_2 in Figure 2e, the lattice spacing of 0.31 nm corresponds to the (111) plane of cubic CeO_2. Figure 2f presents the HRTEM image of the RGO/CeO_2 nanocomposite, in which the interface RGO/CeO_2 is also noticed in addition to the (111) plane of cubic CeO_2. Further characterizations of CeO_2 nanospheres and RGO/CeO_2 nanocomposite by PXRD, EDS, and ATR-FTIR are depicted in Figures S1-S3 of Supporting Information (SI).

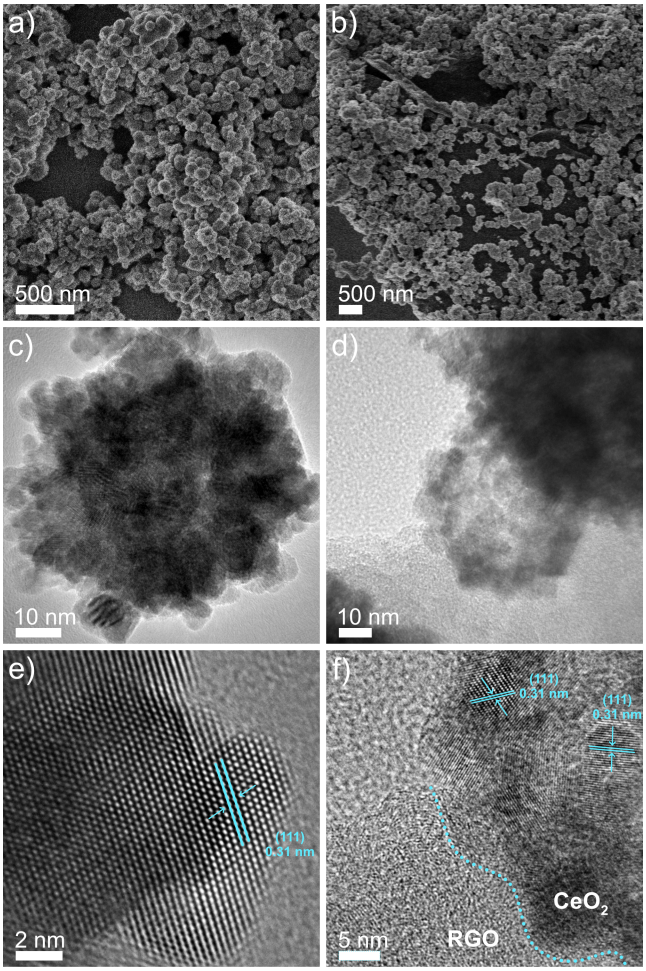

Figure 2. FESEM images of (a) CeO_2 nanospheres, (b) RGO/CeO_2 nanocomposites. TEM images of (c) CeO_2, (d) RGO/CeO_2. HRTEM images of (e) CeO_2, (f) RGO/CeO_2.

The specific surface areas of both materials remain almost unchanged despite the presence of RGO in the RGO/CeO_2 nanocomposite. The specific surface area obtained by the BET method of CeO_2 nanospheres is 34.3 $m^2\ g^{-1}$, whereas RGO/CeO_2 nanocomposite presents an area of 36.5 $m^2\ g^{-1}$. Similar specific surface areas suggest that the CeO_2 nanospheres are distributed on the RGO sheets, as seen in the FESEM image.

To obtain the size distribution of the nanoparticles, we fit the experimental and calculated pair distribution functions (PDFs) for both samples by using the crystallographic data of cubic CeO_2 from the Inorganic Crystal Structure Database (ICSD: 72155) (for details, see notes in SI, Table S1, and Figure S4). The refinement of the spherical particle diameter (sp-diameter) parameters provides values of 114 Å (fraction of 71.5%) and 22 Å (fraction of 28.5%) for pure CeO_2 nanospheres. Whereas the sp-diameter parameters refine to 105 Å (fraction of 66.7%) and 26 Å (fraction of 33.3%) for the RGO/CeO_2 nanocomposite. These results indicate

a size distribution of coherent domains within the range of about 20-120 Å. The sizes of the crystallites are in good agreement with the size of the small nanoparticles visible in TEM images. Moreover, the use of GO as a precursor in the RGO/CeO_2 synthesis does not affect the crystal formation of CeO_2 nor significantly impacts the particle size distribution.

We perform XPS to study the chemical composition of the material's surface. As depicted in Figure 3a, the XPS spectra of pure CeO_2 nanospheres and RGO/CeO_2 exhibit only emissions from cerium, oxygen, and carbon, indicating the purity of the samples. The survey XPS spectra provide a relative quantification of 24.2 at% Ce, 42.7 at% O, and 33.1 at% C for CeO_2, while RGO/CeO_2 nanocomposite has 23.0 at% Ce, 41.0 at% O, and 36.0 at% C. Emissions from carbon in XPS are known to result from atmospheric contamination; thus, the technique is not suitable for the identification of carbon in the nanocomposites with such a small quantity of RGO, and it is not straightforward to assign the small increase in carbon quantification in the nanocomposite to the presence of RGO.

As shown in Figure 3b, the high-resolution XPS spectra at the C 1s energy level of both samples can be fitted in four components C-C/C=C (284.8 eV), C-O (286.3 eV for CeO_2 and 286.9 eV for RGO/CeO_2), O=C-O (289.1 eV), and carbonate-related species (291.5 eV for CeO_2 and 291.1 eV for RGO/CeO_2)[47,48] with similar relative quantities. Except for the carbonate-related component, such contributions are typical of adventitious carbon contamination, but have also been previously reported as contributions of graphene-derived materials.[47,49] Thus, such ambiguous determination of the C 1s components confirms that XPS is not suitable to prove the existence or the oxidation degree of RGO in our nanocomposite.

The XPS core-level spectra of O 1s of both samples, shown in Figure 3c, exhibit an asymmetric peak that suggests three distinct oxygen species. The contribution at 529.1/529.2 eV is assigned to the O^{2-} species from the CeO_2 lattice, the peak at 531.3 eV corresponds to the hydroxyl or carbonate species adsorbed on the surface,[48,50] and the component at 533.7/533.8 eV can be attributed to oxygen bonded to carbon.[51] The hydroxyl and carbonate species on the materials' surface might be residues of the synthetic route, which employs urea, and should be easily removed upon heating before the sensing tests.

As depicted in Figure 3d, both samples exhibit the Ce 3d XPS spectra composed of five doublets due to the multiplet splitting of the Ce $3d_{5/2}$ and Ce $3d_{3/2}$ spin-orbit components. The peaks labeled as v and u correspond to $3d_{5/2}$ and Ce $3d_{3/2}$, respectively, and the fitting into ten components suggests both Ce^{4+} and Ce^{3+} oxidation states on the samples' surfaces. The doublets v and u at 882.1 eV and 900.6 eV, v''and u'' at 888.5 eV and 907.1 eV, and v'''and u''' at

897.7 eV and 916.4 eV correspond to Ce^{4+}, whereas the doublets named v_0 and u_0 at 879.7 eV and 898.4 eV, and v' and u' at 885.0 eV and 903.6 eV are assigned to Ce^{3+}.[50]

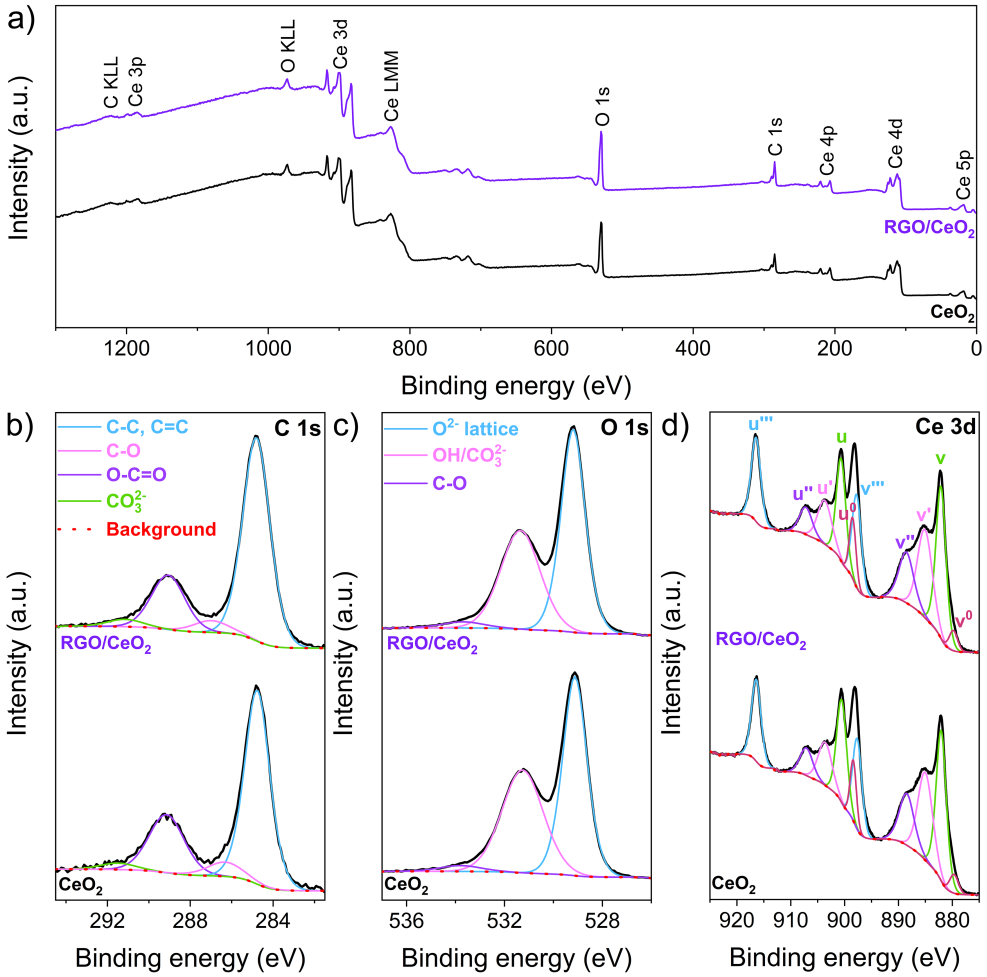

Figure 3. XPS characterization of CeO_2 and RGO/CeO_2 nanocomposite. (a) Survey XPS spectra. XPS spectra measured at the (b) C 1s energy. (c) O 1s energy, and (d) Ce 3d energy, where the v^0, u^0, v', and u' are assigned to Ce^{3+}.

Raman spectroscopy is a powerful tool to identify RGO in our nanocomposite, as shown in Figure 4. The Raman spectrum evidences two characteristic peaks of graphene-based materials denoted as D and G bands for the RGO/CeO_2 nanocomposite. The D band at ~1352 cm^{-1} corresponds to structural defects in the hexagonal graphene framework (e.g., sp^3 hybridized carbons),[47,52] whereas the G band at ~1605 cm^{-1} is assigned to the E_{2g} vibration mode of sp^2 hybridized carbons in the graphitic region.[53] The intensity ratio of D to G bands (I_D/I_G) is about 1.01 for the RGO/CeO_2 nanocomposite. Such a value is higher than the I_D/I_G of 0.88 of the precursor GO,[43] confirming its reduction to RGO during the microwave-assisted

synthesis.[54] Moreover, both pure CeO_2 nanospheres and RGO/CeO_2 nanocomposite exhibit a peak at ~460 cm^{-1} that is assigned to the F_{2g} mode of cubic CeO_2, concerning the O-Ce-O stretching.[55]

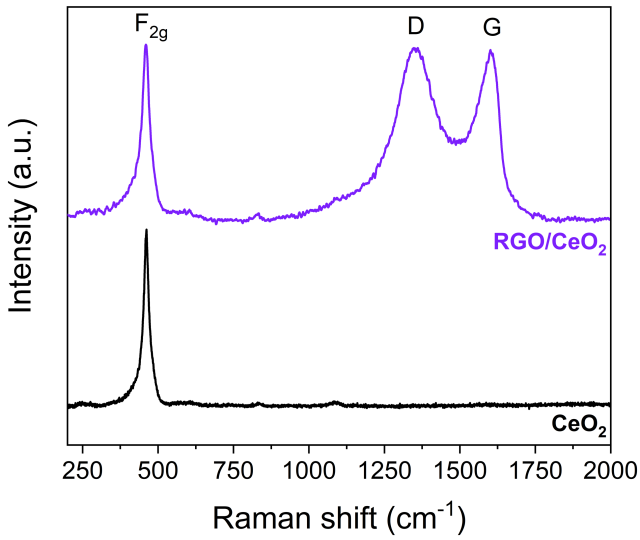

Figure 4. Raman spectra of CeO_2 and the RGO/CeO_2 nanocomposite.

3.2 VOC-Sensing performance

We assess the TEA-sensing performance of CeO_2 nanospheres and RGO/CeO_2 nanocomposites at RT and 34%, 56%, and 70% RH. As depicted in Figure 5, we evaluate the sensing performance of both materials towards TEA by monitoring the changes in the resistance upon exposure to TEA in the concentration range from 5 to 200 ppm. At all RH conditions, both CeO_2 nanospheres and RGO/CeO_2 nanocomposite exhibit high sensitivity to all TEA concentrations and show great reversibility since the electrical resistances can return to their initial resistance after each exposure to TEA. These results are uncommon for SMOx-based sensors but desired for practical applications.

The electrical resistance of the sensors decreases by increasing the RH from 34% to 70%. The magnitude order of the resistance of RGO/CeO_2 nanocomposite changes from GΩ to MΩ (Figure 5d,e,f). Such behavior can be related to the donation of electrons from molecules of water that adsorb to the sensing material,[56] or the interaction of water with the ionosorbed oxygen species on the surface of the material, releasing electrons back to the semiconducting material.[57] Notably, the RGO/CeO_2 nanocomposite shows electrical resistance *ca*. 3.2-4.7 times lower than bare CeO_2 at all RH range. As shown previously, RGO has a lower work

function than CeO_2,[58,59] causing the charge transfer from the RGO to CeO_2. The electron transfer occurs until reaching the Fermi level equilibrium, resulting in a synergistic effect of the combination of the SMOx and RGO that reflects in the decrease of the electrical resistance of the nanocomposite.

Figure S5a,b exhibit the sensors' signal as a function of the TEA concentration. The signals towards TEA for both sensors increase as increasing the RH, which is advantageous but uncommon for chemoresistive sensors,[60] and the sensors achieve the highest signal at 70% RH. Thus, we elucidate that humidity plays a role in enhancing the sensitivity to TEA instead of hindering the sensing performance.

The sensor signal as a function of TEA concentration at 70% RH is given in Figure 6a. The RGO/CeO_2 nanocomposite has superior sensitivity compared to CeO_2 nanospheres for all TEA concentrations. For 200 ppm TEA, the sensor signal of RGO/CeO_2 nanocomposite is ~64% higher than that of CeO_2 nanospheres. We hypothesize that the enhancement in the sensitivity of RGO/CeO_2 occurs not only due to the improvements in the electrical resistance of the sensor but also to the increase in the active sites for TEA adsorption.

The relationship between the logarithm of the sensor signal of RGO/CeO_2 and the logarithm of TEA concentration at 70% RH is depicted in Figure S6. The data show a great linear relationship in which the slope of the linear fit corresponds to the sensor sensitivity, as given in the inset of Figure S6. By using the linear fitting, the calculated detection limit of the RGO/CeO_2 nanocomposite is about 1 ppm (see details in SI and Figure S6), while the practical detection limit is 5 ppm due to the sensing measurement setup. The sensor signals as a function of TEA concentration at 34% and 56% RH are shown in Figure S7a,b.

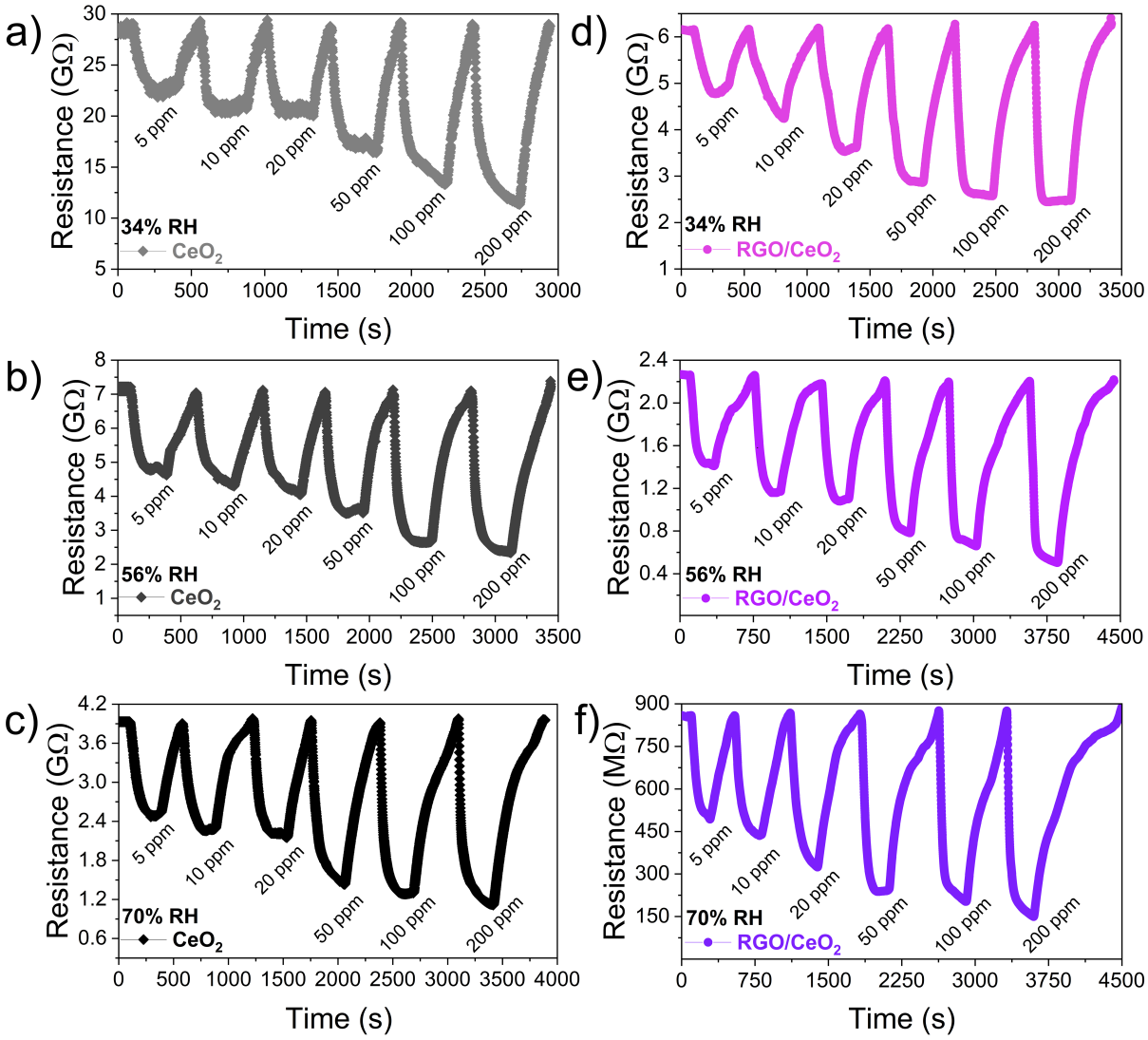

Figure 5. Resistance changes of the sensors during exposure to TEA in the concentration range of 5-200 ppm in humid air at room temperature (RT). (a-c) Variation in the resistance of CeO_2 nanospheres at (a) 34% RH, (b) 56% RH, and (c) 70% RH. (d-e) Changes in the resistance of RGO/CeO_2 nanocomposite at (d) 34% RH, (e) 56% RH, and (f) 70% RH.

The response and recovery times of the sensors are important parameters to be evaluated. We show in Figure 6b,c the response and recovery times of CeO_2 nanospheres and RGO/CeO_2 nanospheres for 100 ppm of TEA at 70% RH. Both sensors have the response and recovery times in the same magnitude order, elucidating that the modification of CeO_2 nanospheres with RGO does not interfere with the speed of response and recovery of the sensor. Nevertheless, both sensors exhibit relatively fast response and recovery times for a chemoresistive sensor operated at RT and humid conditions (see Table 1).

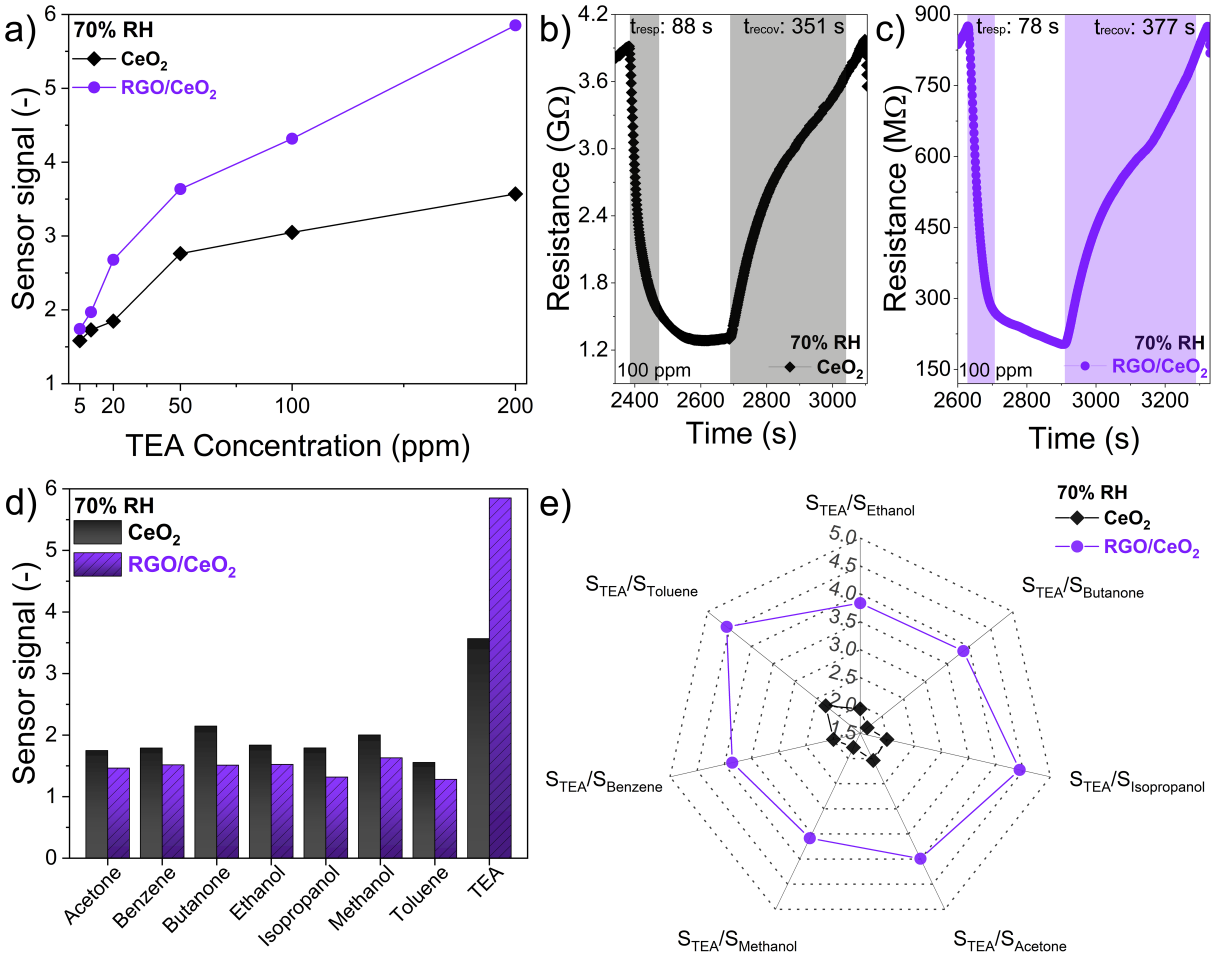

Figure 6. Comparison of the TEA-sensing performance of CeO_2 and RGO/CeO_2 nanocomposite at 70% RH and RT. (a) Sensor signal of both sensors as a function of the TEA concentration. (b) Response and recovery times to 100 ppm of TEA for the CeO_2 nanospheres-based sensor. (c) Response and recovery times to 100 ppm of TEA for the RGO/CeO_2 nanocomposite. (d) Sensor signal to 200 ppm of different testing VOCs. (e) Selectivity of the sensors, showing the ratio S_{TEA}/S_{VOC}, where S_{TEA} is the signal to 200 ppm to TEA and S_{VOC} is the sensor signal to 200 ppm of the testing VOCs.

To illustrate the advantages of the RGO/CeO_2 nanocomposite-based sensor, Table 1 presents the TEA-sensing performance of so far reported chemoresistive sensors. The RGO/CeO_2 nanocomposite has comparable signal and response time to other chemoresistive sensors; however, it operates at RT in humidity conditions. It is clear that high operating temperatures are required to obtain a high sensor signal for many chemoresistive sensors, even for composites-based sensors. Moreover, the sensitivity is achieved in dry conditions, far from practical applications. Thus, we show that our RGO/CeO_2 nanocomposite is a suitable material for highly sensitive TEA detection with low power consumption, in addition to the positive effect of humidity on the sensing performance.

Table 1. Summary of the TEA sensing performance of different chemoresistive sensors.

Sensing Material	Operating temperature (ºC)	RH (%)	Concentration (ppm)	Sensor signal*	Response/recovery times (s)	Ref.
$ZnO/ZnCo_2O_4$	220	26	100	5.12	8/65	[61]
$ZnO/ZnCo_2O_4$	220	45	100	4.0	-/-	[61]
ZnO	40	30	50	2.5	10/21	[62]
Sm doped SnS_2/ZnS	RT	25	100	5.23	8/52	[60]
V_2O_5	370	0	100	7.2	~20/96	[63]
MoS_2/ZnO	RT	0	200	3.43	103/-	[64]
$GaFeO_3$	200	0	200	7.4	9/49	[65]
CuO/Co_3O_4	320	0	200	7.6	68/111	[16]
$Graphene/ZnCo_2O_4$	200	0	100	6.97	45/65	[66]
RGO/CeO_2 nanocomposite	RT	70	100	4.32	78/377	This work

* Sensor signal defined as R_g/R_0 or R_0/R_g

Selectivity is another parameter to be evaluated for practical applications of gas sensors. Figure 6d presents the sensor signal of CeO_2 and RGO/CeO_2 nanocomposite to 200 ppm of several VOCs, including acetone, benzene, butanone, ethanol, isopropanol, methanol, toluene, and TEA. Both sensors are more sensitive to TEA than to the other testing VOCs at 70% RH. The signals to 200 ppm of TEA for CeO_2 and RGO/CeO_2 are 3.57 and 5.85, respectively. The great selectivity and selectivity towards TEA of the CeO_2-based sensors can result from the improved adsorption of TEA molecules on the CeO_2 surface. The TEA molecules have a high electron density around the N atom due to the electron donation of ethyl groups, whereas the surface of CeO_2 contains Ce^{4+} and Ce^{3+} ions.[67] Thus, the interaction between N atoms and Ce ions can facilitate the adsorption of TEA on the sensors' surface and, consequently, increase the sensor signal compared to other VOCs.

As shown in Figure 6e, the signal to TEA reaches values 3.58–4.56 times higher than those to other VOCs for the RGO/CeO_2-based sensor. Such ratios are superior to those seen for pure CeO_2, where the sensor signal to TEA is 1.66–2.29 times higher than those of other testing VOCs. Thus, the RGO/CeO_2 nanocomposite has improved selectivity to TEA, showing another benefit of the modification with RGO. The sensor signals to several testing VOCs at 34% and 56% RH are given in Figure S8.

It is widely accepted that the changes in the resistance of SMOx-based sensors occur due to the oxidation reactions between the reducing VOC and the ionosorbed oxygen species on the surface of the SMOx. When such reactions occur on the surface of an n-type SMOx, the electrons previously captured from the SMOx to form the ionic oxygen species return to the conduction band of the SMOx, resulting in a decrease in the sensor resistance.[68]

Previous studies have shown by using operando DRIFTS that TEA can be partially oxidized or fully converted into CO_2, NO_x, and water, and the TEA-sensing mechanism can occur in more than one step.[28,69,70] Our sensors operate at RT, which might not provide enough activation for the complete TEA oxidation. Moreover, we observe a strong humidity dependence, *i.e.*, the sensitivity improves by increasing humidity levels, suggesting a more complex TEA-sensing mechanism than the oxidation uniquely by the ionosorbed oxygen species. For instance, TEA molecules could interact with water-related surface species. Therefore, in situ mechanistic studies are necessary for the complete understanding of the reactions between the sensors' surface and TEA molecules, which exceeds the scope of this paper.

4. CONCLUSIONS

In summary, we develop a highly sensitive TEA sensor based on RGO/CeO_2 nanocomposite operated at RT and humidity conditions. We demonstrate that pure CeO_2 nanospheres and RGO/CeO_2 nanocomposite are sensitive to TEA with excellent stability and reversibility at RT and RH from 34% to 70%. We observe an improvement in the sensor signal of both sensors upon increasing the RH from 34% to 70%, demonstrating that humidity plays a role in enhancing the sensitivity to TEA instead of hindering the sensing performance. Yet, the RGO/CeO_2 nanocomposite has improved baseline electrical resistance (more than 3 times lower than CeO_2), in addition to the enhanced sensor sensitivity and selectivity to TEA. Moreover, the RGO/CeO_2 shows a low detection limit of 1 ppm at 70% RH and fast response/recovery times for RT conditions, confirming that our nanocomposite has excellent TEA-sensing performance.

Nevertheless, understanding the TEA-sensing mechanism at RT under humid conditions is still needed to develop practical sensors. To reveal the path of TEA oxidation and understand the role of humidity, *in situ* or *operando* mechanistic studies can be carried out. Our findings pave

the way to designing a portable TEA-sensing system that does not require heating elements and can be operated under environmental humidity, which is a first step for developing of advanced and commercial sensors for air quality monitoring and public health.

ACKNOWLEDGMENTS

This work was supported by the São Paulo Research Foundation (FAPESP, grant no. 2018/08271-7, 2016/25267-8, 2018/00033-0, 2017/01267-1, and 2018/01258-5), and the National Council for Scientific and Technological Development (CNPq) – 311453/2021-0 grant. We acknowledge the LMA/IQ/UNESP and LMEOA/IQ/UNICAMP for the FESEM and Raman facilities, respectively, and the Brazilian Nanotechnology National Laboratory−LNNano/CNPEM for the XPS (proposal 24622) and TEM (proposal C1-25112) facilities. Parts of this research were performed at P07 beamline at PETRA III at DESY (Hamburg, Germany), a member of the Helmholtz Association HGF. We thank Dr. Ann-Christin Dippel for supporting the measurements and assistance in the data processing.

Supporting Information

Total scattering experimental details; PXRD patterns; EDS spectra; ATR-FTIR spectra; PDF refinement; sensor signal to TEA at different RH; calculation of the TEA detection limit; sensor signal to various testing VOCs at 34% and 56% RH.

REFERENCES

(1) Stönner, C.; Edtbauer, A.; Williams, J. Real-World Volatile Organic Compound Emission Rates from Seated Adults and Children for Use in Indoor Air Studies. *Indoor Air* **2018**, *28* (1), 164–172. https://doi.org/10.1111/ina.12405.

(2) Mirzaei, A.; Leonardi, S. G.; Neri, G. Detection of Hazardous Volatile Organic Compounds (VOCs) by Metal Oxide Nanostructures-Based Gas Sensors: A Review. *Ceram. Int.* **2016**, *42* (14), 15119–15141. https://doi.org/10.1016/j.ceramint.2016.06.145.

(3) Gandu, B.; Sandhya, K.; Gangagni Rao, A.; Swamy, Y. V. Gas Phase Bio-Filter for the Removal of Triethylamine (TEA) from Air: Microbial Diversity Analysis with Reference to Design Parameters. *Bioresour. Technol.* **2013**, *139*, 155–160. https://doi.org/10.1016/j.biortech.2013.04.030.

(4) Lermantov, S. A.; Velikokhat'ko, T. N.; Zavorin, S. L. Triethylamine as an Effective Catalyst for the Reaction of CO_2 with Epichlorohydrin. *Russ. Chem. Bull.* **1998**, *47* (7), 1405–1406.

(5) OSHA. *Triethylamine*. https://www.osha.gov/chemicaldata/165 (accessed 2021-06-09).

(6) Yang, X.; Yu, Q.; Zhang, S.; Sun, P.; Lu, H.; Yan, X.; Liu, F.; Zhou, X.; Liang, X.; Gao, Y.; Lu, G. Highly Sensitive and Selective Triethylamine Gas Sensor Based on Porous SnO_2/Zn_2SnO_4 Composites. *Sensors Actuators B Chem.* **2018**, *266*, 213–220. https://doi.org/10.1016/j.snb.2018.03.044.

(7) Ju, D.; Xu, H.; Xu, Q.; Gong, H.; Qiu, Z.; Guo, J.; Zhang, J.; Cao, B. High Triethylamine-Sensing Properties of NiO/SnO_2 Hollow Sphere P–N Heterojunction Sensors. *Sensors Actuators B Chem.* **2015**, *215*, 39–44. https://doi.org/10.1016/j.snb.2015.03.015.

(8) Tomer, V. K.; Devi, S.; Malik, R.; Nehra, S. P.; Duhan, S. Highly Sensitive and Selective Volatile Organic Amine (VOA) Sensors Using Mesoporous WO_3–SnO_2 Nanohybrids. *Sensors Actuators B Chem.* **2016**, *229*, 321–330. https://doi.org/10.1016/j.snb.2016.01.124.

(9) Zou, Y.; Chen, S.; Sun, J.; Liu, J.; Che, Y.; Liu, X.; Zhang, J.; Yang, D. Highly Efficient Gas Sensor Using a Hollow SnO_2 Microfiber for Triethylamine Detection. *ACS Sensors* **2017**, *2* (7), 897–902. https://doi.org/10.1021/acssensors.7b00276.

(10) Sá, B. S.; Zito, C. A.; Perfecto, T. M.; Volanti, D. P. Porous $ZnSnO_3$ Nanocubes as a Triethylamine Sensor. *Sensors Actuators B Chem.* **2021**, *338*, 129869. https://doi.org/10.1016/j.snb.2021.129869.

(11) Oliveira, T. N. T.; Perfecto, T. M.; Zito, C. A.; Volanti, D. P. Improved Triethylamine Sensing Properties by Designing an In_2O_3/ZnO Heterojunction. *Sensors and Actuators Reports* **2021**, *3*, 100064. https://doi.org/10.1016/j.snr.2021.100064.

(12) Zhao, Q.; Zhuang, G.; Zhao, Y.; Yang, L.; Zhao, J. Y-Doped In_2O_3 Hollow Nanocubes for Improved Triethylamine-Sensing Performance. *New J. Chem.* **2021**, *45* (15), 6773–6779. https://doi.org/10.1039/D1NJ00452B.

(13) Gui, Y.; Tian, K.; Liu, J.; Yang, L.; Zhang, H.; Wang, Y. Superior Triethylamine Detection at Room Temperature by {-112} Faceted WO_3 Gas Sensor. *J. Hazard. Mater.* **2019**, *380*, 120876. https://doi.org/10.1016/j.jhazmat.2019.120876.

(14) Fan, J.; Yang, C.; Zhao, X.; Li, D.; Xiao, F.; Wu, R.; Wang, L. Enhanced Gas Sensing Property of Co_3O_4 Matrix Nanocomposites with Halloysite Nanotubes toward Triethylamine. *J. Mater. Res. Technol.* **2023**, *23*, 2491–2503. https://doi.org/10.1016/j.jmrt.2023.01.142.

(15) Wang, D.; Zhai, C.; Du, L.; Gu, K.; Zhang, M. Enhanced Triethylamine Sensing Performance of Metal–Organic Framework Derived Nest-Type Fe-Doped NiO Nanostructure. *Inorg. Chem. Front.* **2020**, *7* (6), 1474–1482. https://doi.org/10.1039/D0QI00057D.

(16) Zhao, F.; Hu, C.; Yu, L.; Li, S.; Yin, M.; Fan, X. An Enhanced Triethylamine Response by Incorporating Mesoporous CuO into Nanosheet-Assembled Co_3O_4 Microtubes. *Sensors Actuators B Chem.* **2023**, *379*, 133230. https://doi.org/10.1016/j.snb.2022.133230.

(17) Zhang, Q.; Wang, S.; Fu, H.; Wang, Y.; Yu, K.; Wang, L. Facile Design and Hydrothermal Synthesis of In_2O_3 Nanocube Polycrystals with Superior Triethylamine Sensing Properties. *ACS Omega* **2020**, *5* (20), 11466–11472. https://doi.org/10.1021/acsomega.0c00497.

(18) Xu, X.; Wang, X.; Liu, W.; Wang, S.; Jiang, H.; Ma, S.; Yuan, F.; Ma, N. Triethylamine Gas Sensors Based on BiOBr Microflowers Decorated with ZnO Nanocrystals. *ACS Appl. Nano Mater.* **2022**, *5* (10), 15837–15846. https://doi.org/10.1021/acsanm.2c03997.

(19) Kong, D.; Han, J.; Gao, Y.; Gao, Y.; Zhou, W.; Liu, G.; Lu, G. Lower Coordination Co_3O_4 Mesoporous Hierarchical Microspheres for Comprehensive Sensitization of Triethylamine Vapor Sensor. *J. Hazard. Mater.* **2022**, *430*, 128469. https://doi.org/10.1016/j.jhazmat.2022.128469.

(20) Liu, J.; Zhang, L.; Fan, J.; Zhu, B.; Yu, J. Triethylamine Gas Sensor Based on Pt-Functionalized Hierarchical ZnO Microspheres. *Sensors Actuators B Chem.* **2021**, *331*, 129425. https://doi.org/10.1016/j.snb.2020.129425.

(21) Gao, H.; Ma, Y.; Song, P.; Yang, Z.; Wang, Q. Three-Dimensional Reduced Graphene Oxide/Cobaltosic Oxide as a High-Response Sensor for Triethylamine Gas at Room Temperature. *Mater. Sci. Semicond. Process.* **2021**, *133*, 105904. https://doi.org/10.1016/j.mssp.2021.105904.

(22) Xu, Y.; Zheng, L.; Yang, C.; Zheng, W.; Liu, X.; Zhang, J. Oxygen Vacancies Enabled Porous SnO_2 Thin Films for Highly Sensitive Detection of Triethylamine at Room Temperature. *ACS Appl. Mater. Interfaces* **2020**, *12* (18), 20704–20713. https://doi.org/10.1021/acsami.0c04398.

(23) Sun, H.; Tang, X.; Li, S.; Yao, Y.; Liu, L. MOF-Derived One-Dimensional Ru/Mo Co-Doped Co_3O_4 Hollow Microtubes for High-Performance Triethylamine Sensing. *Sensors Actuators B Chem.* **2023**, *383*, 133583. https://doi.org/10.1016/j.snb.2023.133583.

(24) Zhao, W.; Zhao, Q.; Hao, H.; Lin, H.; Gao, W.; Yan, S. Hydrophobic Modification of WO_3/WS_2 Heterostructure for Construction of Humidity Immune TEA Sensors. *Mater. Chem. Phys.* **2023**, *294*, 126993. https://doi.org/10.1016/j.matchemphys.2022.126993.

(25) Wang, F.; Zhong, H.; Chen, Z.; Wang, D.; Lai, Z.; Deng, Y.; Wang, X. Porous 2D CuO Nanosheets for Efficient Triethylamine Detection at Low Temperature. *Chinese Chem. Lett.* **2023**, *34* (2), 107392. https://doi.org/10.1016/j.cclet.2022.03.115.

(26) Song, X.; Xu, Q.; Zhang, T.; Song, B.; Li, C.; Cao, B. Room-Temperature, High Selectivity and Low-Ppm-Level Triethylamine Sensor Assembled with Au Decahedrons-Decorated Porous α-Fe_2O_3 Nanorods Directly Grown on Flat Substrate. *Sensors Actuators B Chem.* **2018**, *268*, 170–181. https://doi.org/10.1016/j.snb.2018.04.096.

(27) Zhou, S.; Lu, Q.; Chen, M.; Li, B.; Wei, H.; Zi, B.; Zeng, J.; Zhang, Y.; Zhang, J.; Zhu, Z.; Liu, Q. Platinum-Supported Cerium-Doped Indium Oxide for Highly Sensitive Triethylamine Gas Sensing with Good Antihumidity. *ACS Appl. Mater. Interfaces* **2020**, *12* (38), 42962–42970. https://doi.org/10.1021/acsami.0c12363.

(28) Liu, L.; Mao, C.; Fu, H.; Qu, X.; Zheng, S. ZnO Nanorod-Immobilized Pt Single-Atoms as an Ultrasensitive Sensor for Triethylamine Detection. *ACS Appl. Mater. Interfaces* **2023**. https://doi.org/10.1021/acsami.2c21410.

(29) Deng, Z.; Zhang, Y.; Song, Z.; Xu, D.; Zi, B.; Zhu, P.; Lu, Q.; Zhang, J.; Zhao, J.; Liu, Q. Pd-SnO_2/In_2O_3 with a Unique Structure for the Ultrasensitive Detection of Triethylamine near Room Temperature. *ACS Sensors* **2022**, *7* (11), 3501–3512. https://doi.org/10.1021/acssensors.2c01840.

(30) Perfecto, T. M.; Zito, C. A.; Volanti, D. P. Room-Temperature Volatile Organic Compounds Sensing Based on $WO_3 \cdot 0.33H_2O$, Hexagonal-WO_3, and Their Reduced Graphene Oxide Composites. *RSC Adv.* **2016**, *6* (107), 105171–105179. https://doi.org/10.1039/c6ra16892b.

(31) Wei, Q.; Sun, J.; Song, P.; Li, J.; Yang, Z.; Wang, Q. MOF-Derived α-Fe_2O_3 Porous Spindle Combined with Reduced Graphene Oxide for Improvement of TEA Sensing Performance. *Sensors Actuators B Chem.* **2020**, *304*, 127306. https://doi.org/10.1016/j.snb.2019.127306.

(32) Hao, P.; Lin, Z.; Song, P.; Yang, Z.; Wang, Q. RGO-Wrapped Porous $LaFeO_3$ Microspheres for High-Performance Triethylamine Gas Sensors. *Ceram. Int.* **2020**, *46* (7), 9363–9369. https://doi.org/10.1016/j.ceramint.2019.12.194.

(33) Yu, T.; Li, X.; Chen, B.; Yang, Y.; Xu, K.; Liu, Y.; Gong, W.; Yuan, C.; Yang, Y. Enhanced Gas Sensing Performance of RGO Wrapped Crystal Facet-Controlled Co_3O_4 Nanocomposite Heterostructures. *J. Phys. Chem. C* **2022**, *126* (10), 4879–4888. https://doi.org/10.1021/acs.jpcc.2c00598.

(34) Li, P.; Wang, B.; Qin, C.; Han, C.; Sun, L.; Wang, Y. Band-Gap-Tunable CeO_2 Nanoparticles for Room-Temperature NH_3 Gas Sensors. *Ceram. Int.* **2020**, *46* (11), 19232–19240. https://doi.org/10.1016/j.ceramint.2020.04.261.

(35) Liu, J.-S.; Song, B.-Y.; Huang, J.; Deng, Z.-P.; Zhang, X.-F.; Xu, Y.-M.; Huo, L.-H.; Gao, S. Absorbent Cotton Derived Mesoporous CeO_2 Hollow Tubule for Enhanced Detection of P-Xylene at Low Energy Consumption. *J. Alloys Compd.* **2021**, *873*, 159774. https://doi.org/10.1016/j.jallcom.2021.159774.

(36) Zito, C. A.; Perfecto, T. M.; Volanti, D. P. Porous CeO_2 Nanospheres for a Room Temperature Triethylamine Sensor under High Humidity Conditions. *New J. Chem.* **2018**, *42* (19), 15954–15961. https://doi.org/10.1039/C8NJ03300E.

(37) Zito, C. A.; Perfecto, T. M.; Dippel, A.-C.; Volanti, D. P.; Koziej, D. Low-Temperature Carbon Dioxide Gas Sensor Based on Yolk–Shell Ceria Nanospheres. *ACS Appl. Mater. Interfaces* **2020**, *12* (15), 17745–17751. https://doi.org/10.1021/acsami.0c01641.

(38) Su, P.-G.; Lu, W.-Y. One-Pot Synthesis of Plate-like CeO_2 Nanosheets for Sensing NH_3 Gas at Room Temperature. *Mater. Chem. Phys.* **2022**, *277*, 125453. https://doi.org/10.1016/j.matchemphys.2021.125453.

(39) Zhang, L.; Fang, Q.; Huang, Y.; Xu, K.; Chu, P. K.; Ma, F. Oxygen Vacancy Enhanced Gas-Sensing Performance of CeO_2/Graphene Heterostructure at Room Temperature. *Anal. Chem.* **2018**, *90* (16), 9821–9829. https://doi.org/10.1021/acs.analchem.8b01768.

(40) Hu, J.; Zou, C.; Su, Y.; Li, M.; Ye, X.; Cai, B.; Kong, E. S.-W.; Yang, Z.; Zhang, Y. Light-Assisted Recovery for a Highly-Sensitive NO_2 Sensor Based on RGO-CeO_2 Hybrids. *Sensors Actuators B Chem.* **2018**, *270*, 119–129. https://doi.org/10.1016/j.snb.2018.05.027.

(41) Zhang, L.; Zhang, J.; Huang, Y.; Xu, H.; Zhang, X.; Lu, H.; Xu, K.; Chu, P. K.; Ma, F. Stability and Sensing Enhancement by Nanocubic CeO_2 with {100} Polar Facets on Graphene for NO2 at Room Temperature. *ACS Appl. Mater. Interfaces* **2020**, *12* (4), 4722–4731. https://doi.org/10.1021/acsami.9b18155.

(42) Hummers, W. S.; Offeman, R. E. Preparation of Graphitic Oxide. *J. Am. Chem. Soc.* **1958**, *80* (6), 1339–1339. https://doi.org/10.1021/ja01539a017.

(43) Zito, C. A.; Perfecto, T. M.; Mazon, T.; Dippel, A.-C.; Koziej, D.; Volanti, D. P. Reoxidation of Graphene Oxide: Impact on the Structure, Chemical Composition, Morphology and Dye Adsorption Properties. *Appl. Surf. Sci.* **2021**, *567*, 150774. https://doi.org/10.1016/j.apsusc.2021.150774.

(44) Yang, Z.; Wei, J.; Yang, H.; Liu, L.; Liang, H.; Yang, Y. Mesoporous CeO_2 Hollow Spheres Prepared by Ostwald Ripening and Their Environmental Applications. *Eur. J. Inorg. Chem.* **2010**, *2010* (21), 3354–3359. https://doi.org/10.1002/ejic.201000030.

(45) da Silva, E. L.; Varela, J. A.; Almeida, D. K. de A.; Volanti, D. P. Microwave Aided Device for Hydrothermal Synthesis of Nanostructured Oxides, Particularly Obtaining Particles of Metal Oxides, Comprises Container, in Which Hydrothermal Reaction Takes Place, and Lid for Container. Patent BR200815393-A2, December 7, 2010.

(46) Perfecto, T. M.; Volanti, D. P. Gas Sensor Measurement Chamber Manufactured by 3D Printing Useful for Electrical Measurements of Characterization of Materials Comprises Sample Holder to Plug-in Sample Holder and Moisture Control Container Lid with Drilling. Patent BR102019023340-A2, May 18, 2021.

(47) Sofer, Z.; Šimek, P.; Jankovský, O.; Sedmidubský, D.; Beran, P.; Pumera, M. Neutron Diffraction as a Precise and Reliable Method for Obtaining Structural Properties of Bulk Quantities of Graphene. *Nanoscale* **2014**, *6* (21), 13082–13089. https://doi.org/10.1039/C4NR04644G.

(48) Moulder, J. F.; Stickle, W. F.; Sobol, P. E.; Bomben, K. D. *Handbook of X-Ray Photoelectron Spectroscopy: A Reference Book of Standard Spectra for Identification and Interpretation of XPS*; Chastain, J., Ed.; Physical Electronics Division, Perkin-Elmer Corporation, 1992.

(49) Park, S.-H.; Kim, H.-K.; Yoon, S.-B.; Lee, C.-W.; Ahn, D.; Lee, S.-I.; Roh, K. C.; Kim, K.-B. Spray-Assisted Deep-Frying Process for the In Situ Spherical Assembly of Graphene for Energy-Storage Devices. *Chem. Mater.* **2015**, *27* (2), 457–465. https://doi.org/10.1021/cm5034244.

(50) Abi-aad, E.; Bechara, R.; Grimblot, J.; Aboukais, A. Preparation and Characterization of Ceria under an Oxidizing Atmosphere. Thermal Analysis, XPS, and EPR Study. *Chem. Mater.* **1993**, *5* (6), 793–797. https://doi.org/10.1021/cm00030a013.

(51) Joung, D.; Singh, V.; Park, S.; Schulte, A.; Seal, S.; Khondaker, S. I. Anchoring Ceria Nanoparticles on Reduced Graphene Oxide and Their Electronic Transport Properties. *J. Phys. Chem. C* **2011**, *115* (50), 24494–24500. https://doi.org/10.1021/jp206485v.

(52) Eckmann, A.; Felten, A.; Mishchenko, A.; Britnell, L.; Krupke, R.; Novoselov, K. S.; Casiraghi, C. Probing the Nature of Defects in Graphene by Raman Spectroscopy. *Nano Lett.* **2012**, *12* (8), 3925–3930. https://doi.org/10.1021/nl300901a.

(53) Some, S.; Bhunia, P.; Hwang, E.; Lee, K.; Yoon, Y.; Seo, S.; Lee, H. Can Commonly Used Hydrazine Produce N-Type Graphene? *Chem. - A Eur. J.* **2012**, *18* (25), 7665–7670. https://doi.org/10.1002/chem.201200104.

(54) Meng, H.; Yang, W.; Ding, K.; Feng, L.; Guan, Y. Cu_2O Nanorods Modified by Reduced Graphene Oxide for NH3 Sensing at Room Temperature. *J. Mater. Chem. A* **2015**, *3* (3), 1174–1181. https://doi.org/10.1039/C4TA06024E.

(55) Sánchez Escribano, V.; Fernández López, E.; Panizza, M.; Resini, C.; Gallardo Amores, J. M.; Busca, G. Characterization of Cubic Ceria–Zirconia Powders by X-Ray Diffraction and Vibrational and Electronic Spectroscopy. *Solid State Sci.* **2003**, *5* (10), 1369–1376. https://doi.org/10.1016/j.solidstatesciences.2003.07.001.

(56) Boyle, J. F.; Jones, K. A. The Effects of CO, Water Vapor and Surface Temperature on the Conductivity of a SnO_2 Gas Sensor. *J. Electron. Mater.* **1977**, *6* (6), 717–733. https://doi.org/10.1007/BF02660346.

(57) Chen, Z.; Lu, C. Humidity Sensors: A Review of Materials and Mechanisms. *Sens. Lett.* **2005**, *3* (4), 274–295. https://doi.org/10.1166/sl.2005.045.

(58) Xu, L.; Huang, W.-Q.; Wang, L.-L.; Huang, G.-F. Interfacial Interactions of Semiconductor with Graphene and Reduced Graphene Oxide: CeO_2 as a Case Study. *ACS Appl. Mater. Interfaces* **2014**, *6* (22), 20350–20357. https://doi.org/10.1021/am5058772.

(59) Naganaboina, V. R.; Singh, S. G. Graphene-CeO_2 Based Flexible Gas Sensor: Monitoring of Low Ppm CO Gas with High Selectivity at Room Temperature. *Appl. Surf. Sci.* **2021**, *563*, 150272. https://doi.org/10.1016/j.apsusc.2021.150272.

(60) Li, F.; Zeng, Z.; Wu, M.; Liu, L.; Li, W.; Huang, F.; Li, W.; Guan, H.; Geng, W. Room-Temperature Triethylamine Sensing of a Chemiresistive Sensor Based on Sm-Doped SnS2/ZnS Hierarchical Microspheres. *New J. Chem.* **2022**, *46* (32), 15701–15711. https://doi.org/10.1039/D2NJ02683J.

(61) Li, Y.; Luo, N.; Sun, G.; Zhang, B.; Jin, H.; Lin, L.; Bala, H.; Cao, J.; Zhang, Z.; Wang, Y. Synthesis of Porous Nanosheets-Assembled ZnO/$ZnCo_2O_4$ Hierarchical Structure for TEA Detection. *Sensors Actuators B Chem.* **2019**, *287*, 199–208. https://doi.org/10.1016/j.snb.2019.02.055.

(62) Song, X.; Xu, Q.; Xu, H.; Cao, B. Highly Sensitive Gold-Decorated Zinc Oxide Nanorods Sensor for Triethylamine Working at near Room Temperature. *J. Colloid Interface Sci.* **2017**, *499*, 67–75. https://doi.org/10.1016/j.jcis.2017.03.092.

(63) Wu, M.; Zhang, X.; Gao, S.; Cheng, X.; Rong, Z.; Xu, Y.; Zhao, H.; Huo, L. Construction of Monodisperse Vanadium Pentoxide Hollow Spheres via a Facile Route and Triethylamine Sensing Property. *CrystEngComm* **2013**, *15* (46), 10123. https://doi.org/10.1039/c3ce41471j.

(64) Xu, X. L.; Wang, X. P.; Chen, Y.; Liu, W. W.; Wang, S. Y.; Yuan, F. Q.; Ma, S. Y. Design of MoS_2/ZnO Bridge-like Hetero-Nanostructures to Boost Triethylamine (TEA) Sensing. *Vacuum* **2022**, *196*, 110733. https://doi.org/10.1016/j.vacuum.2021.110733.

(65) Yu, Q.; Kong, W.; Zhang, Y.; Li, X.; Xu, Y. Morphology-Controllable Synthesis of Hierarchical Hollow $GaFeO_3$ Microcubes with Selective Triethylamine Gas-Sensing Properties. *Ceram. Int.* **2022**, *48* (4), 4554–4562. https://doi.org/10.1016/j.ceramint.2021.10.241.

(66) Ebrahimi, M.; Soleimanian, V.; Ghasemi, M.; Nekoeinia, M.; Mokhtari, A. Effects of Graphene Quantum Dots on Microstructure, Optical and Gas Sensing Properties of Coral-like $ZnCo_2O_4$ Nanoparticles. *Phys. B Condens. Matter* **2023**, *650*, 414439. https://doi.org/10.1016/j.physb.2022.414439.

(67) Zhang, L.; Zhao, J.; Lu, H.; Li, L.; Zheng, J.; Zhang, J.; Li, H.; Zhu, Z. Highly Sensitive and Selective Dimethylamine Sensors Based on Hierarchical ZnO Architectures Composed of Nanorods and Nanosheet-Assembled Microspheres. *Sensors Actuators B Chem.* **2012**, *171–172*, 1101–1109. https://doi.org/10.1016/j.snb.2012.06.040.

(68) Gurlo, A. Interplay between O_2 and SnO_2: Oxygen Ionosorption and Spectroscopic Evidence for Adsorbed Oxygen. *ChemPhysChem* **2006**, *7* (10), 2041–2052. https://doi.org/10.1002/cphc.200600292.

(69) Lou, C.; Wang, K.; Liu, X.; Li, X.; Wang, H.; Li, L.; Zheng, W.; Zhang, J. Heterogeneous Co_3O_4/Carbon Nanofibers for Low Temperature Triethylamine Detection: Mechanistic Insights by Operando DRIFTS and DFT. *Adv. Mater. Interfaces* **2022**, *9* (1), 2101479. https://doi.org/10.1002/admi.202101479.

(70) Li, G.; Ma, Z.; Hu, Q.; Zhang, D.; Fan, Y.; Wang, X.; Chu, X.; Xu, J. PdPt Nanoparticle-Functionalized α-Fe_2O_3 Hollow Nanorods for Triethylamine Sensing. *ACS Appl. Nano Mater.* **2021**, *4* (10), 10921–10930. https://doi.org/10.1021/acsanm.1c02377.